

Synthetic Mimics of Native Siderophores Disrupt Iron Trafficking in *Acinetobacter baumannii*Tabbatha J. Bohac,[§] Luting Fang,[§] Victoria S. Banas,[§] Daryl E. Giblin, and Timothy A. Wencewicz*Cite This: <https://doi.org/10.1021/acsinfectdis.1c00119>

Read Online

ACCESS |



Metrics & More



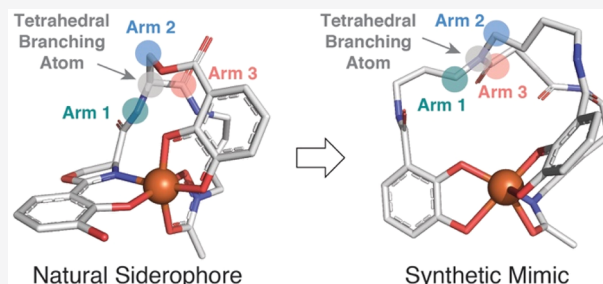
Article Recommendations



Supporting Information

ABSTRACT: Many pathogenic bacteria biosynthesize and excrete small molecule metallophores, known as siderophores, that are used to extract ferric iron from host sources to satisfy nutritional need. Native siderophores are often structurally complex multidentate chelators that selectively form high-affinity octahedral ferric iron complexes with defined chirality recognizable by cognate protein receptors displayed on the bacterial cell surface. Simplified achiral analogues can serve as synthetically tractable siderophore mimics with potential utility as chemical probes and therapeutic agents to better understand and treat bacterial infections, respectively. Here, we demonstrate that synthetic spermidine-derived mixed ligand bis-catecholate monohydroxamate siderophores (compounds 1–3) are versatile structural and biomimetic analogues of two native siderophores, acinetobactin and fimsbactin, produced by *Acinetobacter baumannii*, a multidrug-resistant Gram-negative human pathogen. The metal-free and ferric iron complexes of the synthetic siderophores are growth-promoting agents of *A. baumannii*, while the Ga(III)-complexes are potent growth inhibitors of *A. baumannii* with MIC values $<1 \mu\text{M}$. The synthetic siderophores compete with native siderophores for uptake in *A. baumannii* and maintain comparable apparent binding affinities for ferric iron (K_{Fe}) and the siderophore-binding protein BauB (K_{d}). Our findings provide new insight to guide the structural fine-tuning of these compounds as siderophore-based therapeutics targeting pathogenic strains of *A. baumannii*.

KEYWORDS: *Acinetobacter baumannii*, virulence, antibiotic, resistance, iron, siderophore



Bacterial infections caused by multidrug-resistant (MDR) Gram-negative pathogens are on the rise.^{1,2} This alarming trend is further complicated by the difficulty of discovering new antibiotic scaffolds active against Gram-negative bacteria due primarily to the restricted permeability of the cell envelope toward small molecules.^{3,4} Siderophore-based therapeutics overcome this inherent permeability barrier by gaining cell entry *via* TonB-dependent receptor-mediated uptake pathways required for bacterial iron acquisition.⁵ Bacterial pathogens including MDR Gram-negatives often rely on siderophores,^{6,7} small molecule ferric iron chelators, and cell-associated receptor proteins to extract iron from host sources.⁸ Hence, siderophores are considered virulence factors required for Gram-negative pathogens to establish, maintain, and propagate the infection.^{9,10}

Pathogen-produced siderophores represent attractive small molecule scaffolds that can serve as chassis for pathogen-targeted siderophore-based therapeutics.⁵ Four general approaches for siderophore-based therapeutics have been reported: (1) siderophore–antibiotic conjugates (sideromycins) for targeted drug delivery;^{5,11} (2) siderophore–metal chelates for delivery of toxic or radioactive metals;^{12,13} (3) small molecule inhibitors of siderophore biosynthetic enzymes,^{14–16} and (4) competitive agonists and antagonists of siderophore receptors, transporters, and binding pro-

teins.^{17–19} These approaches often rely on the use of a siderophore-like compound or a siderophore-derived fragment to gain cell entry against a target pathogen that utilizes and likely possesses innate biosynthetic capacity for the parent siderophore. Hence, the *in vivo* efficacy of siderophore-based therapeutics depends on the ability of the modified siderophore to outcompete a pathogen's native siderophore(s) for cell entry *via* a conditionally essential siderophore system that is not easily compensated by other pathways or deleted entirely.

Natural siderophores are chiral and often structurally complex molecules.⁷ The total chemical synthesis or semisynthesis of natural siderophores and analogues suitable for functionalization, while an incredibly valuable exercise, can be time-consuming and mass limiting.^{20–22} The use of simplified siderophore structural mimics that are synthetically accessible and scalable is an attractive alternative that can still leverage

Special Issue: Antibiotic Alternatives

Received: March 9, 2021

the benefits (increased potency and selectivity) of siderophore-based therapeutics.¹¹ Many multidentate ferric iron chelators containing catechol, hydroxamate, and carboxylate ligands (common to most siderophores) have been reported in the literature, and some have proven to be useful as sideromycin antibiotic delivery vectors.⁵

In 1996, the Miller group reported a mixed ligand biscatecholate monohydroxamate siderophore **1** synthesized from a spermidine backbone (Figure 1).²³ In this synthetic

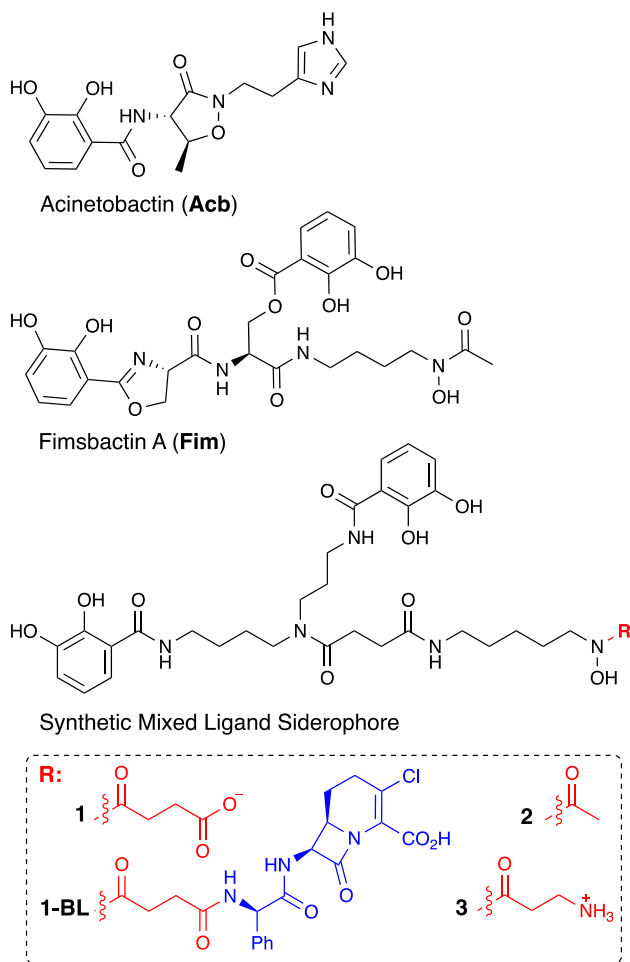


Figure 1. Chemical structures of natural *A. baumannii* siderophores fimsbactin A (Fim)/acinetobactin (Acb), synthetic mixed ligand siderophores **1–3**, and synthetic mixed ligand sideromycin **1-BL**.

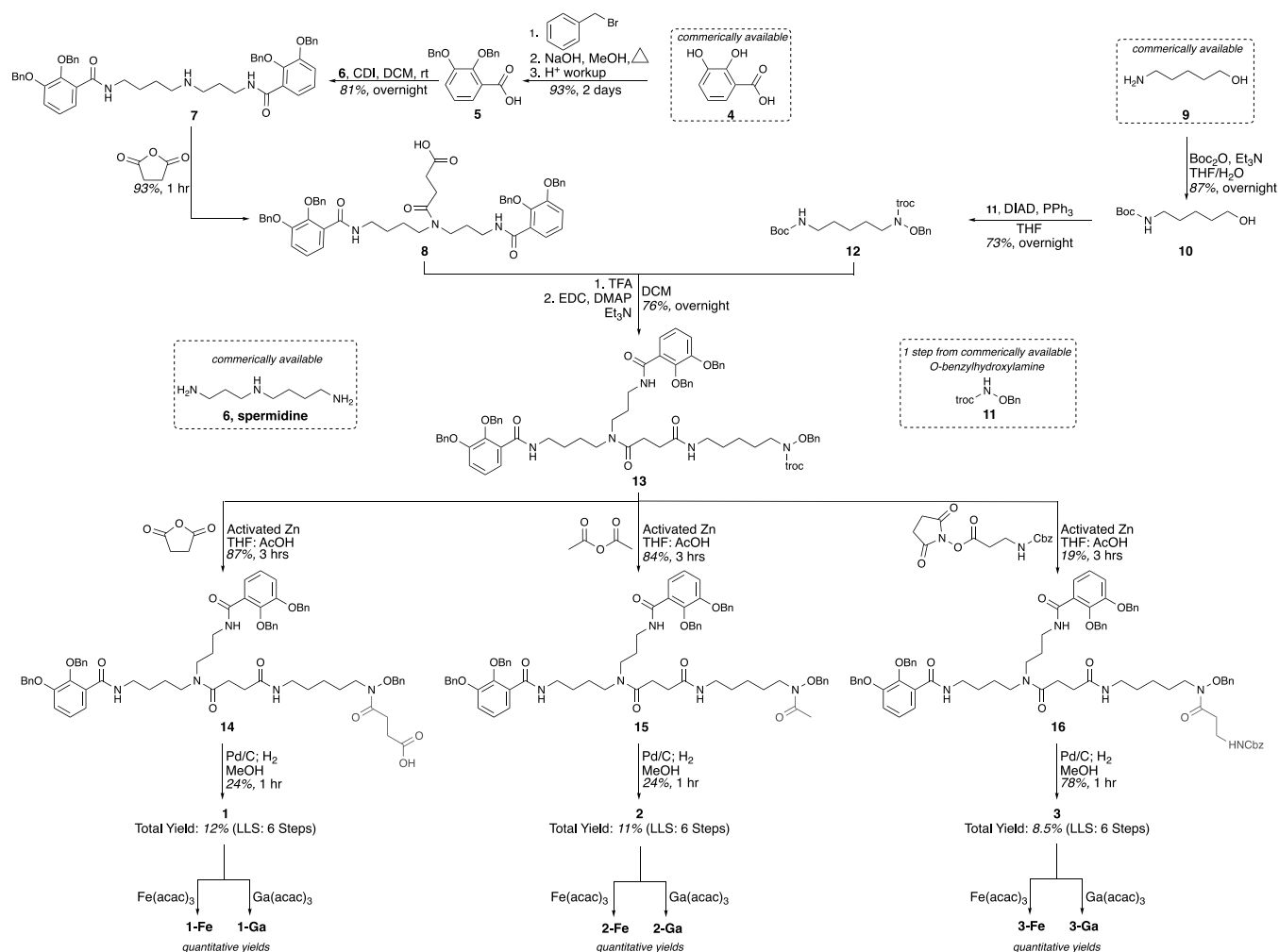
siderophore, N_1 and N_{10} are acylated with 2,3-dihydroxybenzoic acid (DHB) and N_5 is succinylated to provide a branch point. Branching was achieved by amide bond formation between the free carboxylate of the succinyl group and the primary amino group of N_1 -hydroxy- N_1 -succinyl-cadaverine. This completed the mixed ligand siderophore scaffold and provided an additional site for functionalization in the succinyl group of the cadaverine hydroxamate unit. The beta-lactam antibiotic loracarbef, a carbacephalosporin, was covalently linked to the mixed ligand siderophore via a stable amide bond between the cadaverine succinyl group and the free amino group of loracarbef's 2-amino-phenylacetic acid side chain to provide mixed ligand beta-lactam sideromycin **1-BL** (Figure 1).

Broad antimicrobial testing of mixed ligand sideromycin **1-BL** serendipitously revealed incredible potency ($\text{MIC}_{90} = 0.03$

$\mu\text{g/mL}$) against MDR *Acinetobacter baumannii* with only moderate potency (16–128 $\mu\text{g/mL}$) against other Gram-negative and Gram-positive pathogens.²³ The origins of this impressive potency and selectivity toward *A. baumannii* was not entirely clear, although it was proposed that sideromycin **1-BL** was utilizing siderophore uptake pathways unique to *A. baumannii*. This was later confirmed in 2013 when the Miller group revisited these compounds in siderophore–sideromycin competition assays that revealed the parent siderophore was controlling translocation of the sideromycin to the periplasm where the target penicillin-binding proteins could be inhibited by the loracarbef moiety.¹¹ Since 2013, the Miller group has shown that mixed ligand siderophore **1**, containing either a succinyl or glutaryl *N*-acyl-hydroxamate linker, is a versatile antibiotic,²⁴ biosensor,²⁵ and drug delivery vector for targeting *A. baumannii* with a wide variety of antibiotics that act on periplasmic targets including beta-lactams,^{11,23} lipodepsipeptides,^{26,27} and glycopeptides.^{28,29} Attempts to utilize siderophore **1** to deliver antibiotics with cytoplasmic targets, such as fluoroquinolones, have failed, implying that this siderophore scaffold is transported to the periplasm but not the cytoplasm.¹¹ Several groups, including the Miller,^{30–32} Nolan,^{33–35} and Seiple³⁶ groups, have made recent advancements in developing cleavable linker systems for siderophore–antibiotic conjugates enabling pathogen-triggered drug release to expand this drug delivery technology to antibiotics with cytoplasmic targets.³⁷

Growing evidence from biological testing data suggests that sideromycins derived from mixed ligand siderophore **1** are transported via a siderophore pathway that is unique to pathogenic *A. baumannii* strains, explaining the unique and potent selectivity of these antibiotics toward this pathogen.^{11,23} Human pathogenic *A. baumannii* can produce up to three siderophores, including fimsbactins (Fim),³⁸ acinetobactin (Acb),³⁹ and baumannoferrin.⁴⁰ In 2013, the Bode group disclosed the structure of the novel mixed ligand siderophore **Fim** isolated from an environmental strain of *A. baylyi* (Figure 1).³⁸ In 2019, our group isolated **Fim** from two pathogenic strains of *A. baumannii*.⁴¹ Genome mining and *in vivo* studies revealed that the fimsbactins may have been functionally replaced in the *Acinetobacter* genome by the strictly conserved NRPS siderophore **Acb** which shares some structural and biosynthetic similarity to the fimsbactins.^{41–43} **Acb** is derived from the pH-dependent isomerization of the NRPS product preacinetobactin and has been shown to be the exclusive siderophore needed to enhance virulence in *A. baumannii* mouse infection models.^{43,44} Our group has developed synthetic structural mimics of **Acb** and preacinetobactin that can disrupt siderophore-mediated iron acquisition in *A. baumannii* as an antivirulence strategy.^{17,45} Subsequently, we demonstrated that **Fim** effectively outcompetes native preacinetobactin and **Acb** for receptor-mediated transport to the periplasm, making this an attractive siderophore chassis for the development of siderophore-based therapeutics against *A. baumannii*.⁴¹

The native *A. baumannii* siderophore **Fim** is derived from a nonribosomal peptide synthetase (NRPS) biosynthetic assembly line and utilizes L-Ser as the central tetrahedral branching unit for two catecholates and one hydroxamate.³⁸ This shows structural similarities with the biscatecholate monohydroxamate ligand pattern of the synthetic siderophore analogue **1**, which is built on a central spermidine tetrahedral branching unit providing the first clue on the origins of the impressive

Scheme 1. Synthesis of Mixed Ligand Siderophores 1, 2, and 3 and the Corresponding 1:1 Chelation Complexes with Fe(III) (1-Fe, 2-Fe, and 3-Fe) and Ga(III) (1-Ga, 2-Ga, and 3-Ga)


selectivity of this compound for *A. baumannii* as a potential **Fim** mimic.^{11,23} In this work, we provide the first direct evidence that mixed ligand siderophore **1** is in fact a true **Fim** mimic. Siderophore **1** can outcompete native siderophores **Acb** and **Fim** for translocation to the periplasm in MDR *A. baumannii* where it binds to the siderophore-binding protein BauB. Additionally, we reveal the structural basis for ferric iron chelation and receptor recognition leading to active transport across the outer membrane. Our findings validate and guide the utility and design, respectively, of mixed ligand siderophore **1** and hydroxamate *N*-acyl analogues **2** and **3** (Figure 1) as effective chassis for pathogen-targeted siderophore-based therapeutics against infections caused by MDR *A. baumannii* pathogens.

RESULTS AND DISCUSSION

Design and Synthesis of Mixed Ligand Siderophores.

The fimsbactin siderophores are produced as a mixture of NRPS products known as fimsbactin A–F.³⁸ Our group and others have shown that fimsbactin A (referred to simply as **Fim** from this point forward) is the primary mass component of the fimsbactin mixture and seems to be the dominant biologically active siderophore metabolite.⁴¹ The mixed ligand siderophore **1** mimics the structure of fimsbactin A with two catecholates and one hydroxamate ferric iron chelating groups yet lacks the

two chiral centers present in **Fim**, including the chiral branching point created by *L*-Ser. Spermidine serves as the structural backbone of siderophore **1** and is found in naturally occurring siderophores such as vibrobactin produced by *Vibrio cholerae*.⁴⁶ The triamine functionality of spermidine provides useful synthetic handles for the synthesis of tripodal siderophore mimics containing different iron chelating functional groups including catecholates and hydroxamates with control of ligand orientations with respect to iron chelation. The free carboxylate of the *N*-succinoyl-hydroxamate serves as a useful attachment site for molecular cargo, including antibiotics, and does not seem to interfere with iron binding or receptor-mediated transport.¹¹

The free carboxylate of compound **1** ensures that the net charge of the metal-free and the ferric iron complex are anionic at physiological pH. Our group has previously shown that the net charge of siderophores influences their uptake through siderophore pathways presumably through electrostatic effects. For the Gram-positive pathogen *Staphylococcus aureus* and the ferric hydroxamate siderophore-binding lipoprotein FhuD2 we found that neutral and cationic hydroxamate siderophores were the most efficient growth promoters and displayed the highest apparent affinity for binding to protein receptors.⁴⁷ We sought to probe electrostatic effects of compound **1** by preparing two additional *N*-acyl-hydroxamate analogues **2** and

3 containing a charge neutral acetyl group and a cationic 3-amino-propanoyl group, respectively (Figure 1).

To prepare mixed ligand siderophores **1**, **2**, and **3**, we adapted a synthetic route based on the convergent strategy originally reported by the Miller group utilizing fully protected intermediate **13** that can readily be functionalized with different *N*-acyl-hydroxamate groups through selective removal of the 2,2,2-trichloroethoxycarbonyl (Troc) protecting group (Scheme 1).^{11,23,28} Compound **13** was synthesized from four commercially available starting materials: (1) DHB (**4**), (2) spermidine (**6**), (3) 5-amino-1-pentanol (**9**), and (4) *O*-benzylhydroxylamine. Universal benzyl protection of **4** with benzyl bromide followed by saponification of the benzyl ester provided carboxylate **5** that can be coupled directly with spermidine **6** via amide bond formation with the two primary amines facilitated by carbonyldiimidazole (CDI) to give compound **7**. Acylation of the secondary amine with succinic anhydride in the presence of a 4-dimethylaminopyridine (DMAP) catalyst provided the first major fragment, compound **8**. The second major fragment **12** facilitating convergent synthesis of compound **13** was synthesized starting from 5-amino-1-pentanol **9**. Tertbutyloxycarbonyl (Boc) protection of the primary amine provided compound **10**, and subsequent Mitsunobu reaction with *N*-Troc-*O*-benzylhydroxylamine **11** (available in one-step from commercially available *O*-benzylhydroxylamine) provided compound **12**. Boc deprotection of **12** and amide bond coupling with the free succinoyl carboxyl group of **8** provided compound **13**. All reactions can be performed on gram scale to provide gram quantities of **13** in good overall yield (53% for LLS).

With gram quantities of compound **13** in hand, we performed a series of one-pot Troc-deprotection and acyl group transfers to prepare compounds **14**–**16**.⁴⁸ Treatment of **13** with activated Zn in the presence of succinic anhydride and acetic acid provided *N*-succinoyl intermediate **14**. Treatment of **13** with activated Zn, acetic anhydride, and acetic acid provided *N*-acetyl intermediate **15**. Treatment of **13** with activated Zn and the *N*-hydroxysuccinimide (NHS)-ester of benzyloxycarbonyl (Cbz)-protected 3-aminopropionic acid in the presence of acetic acid provided *N*-propanoyl derivative **16**. Compounds **14**–**16** were rigorously purified by prep-HPLC prior to global benzyl/Cbz deprotection using Pd-catalyzed hydrogenolysis to provide the final metal-free siderophores **1**–**3** in high enough purity (>90%) to facilitate complete characterization and biological testing. For context, the first total synthesis of **Fim** was completed by Kim and co-workers in 2020, providing an elegant route completed in 16 steps and 5% overall yield that is somewhat limited by epimerization of the oxazoline stereocenter.^{49,50} Mixed ligand **Fim** mimics **1**–**3** can be prepared in fewer steps, higher yield, and greater mass with no concern of chirality (Scheme 1).

Ferric Iron Chelation by Mixed Ligand Siderophores.

The ability to form stable high-affinity chelation complexes with ferric iron under physiological conditions is a critical property for all siderophores.⁷ We prepared the Fe(III) complexes (**1-Fe**, **2-Fe**, and **3-Fe**) and Ga(III) complexes (**1-Ga**, **2-Ga**, and **3-Ga**) of siderophores **1**–**3** by treatment with stoichiometric Fe(acac)₃ or Ga(acac)₃, respectively, in a methanolic solution followed by trituration with diethyl ether to remove excess acac ligand (Scheme 1). The compounds formed stable complexes with both Ga(III) and Fe(III) consistent with previous reports utilizing Ga(III) as a redox stable Fe(III) surrogate.^{12,13} Compound **1** was shown

previously to form a stable 1:1 ligand:Fe(III) complex with apparent log $K_{Fe} = 27.0$.^{11,51} Thus, assuming 1:1 ligand:Fe(III) stoichiometry, we utilized a competition experiment with excess EDTA (1.2 equiv) to determine the apparent ferric iron binding affinity values (K_{Fe}) of siderophores **1-Fe**, **2-Fe**, and **3-Fe** based on the known apparent K_{Fe} value of $10^{25.1}$ for EDTA-Fe determined at pH 7.4 (Table 1).⁵² On the basis of data

Table 1. Apparent Ferric Iron Binding Properties and BauB Dissociation Constants for Siderophores and Mimics

compound	ligand:Fe(III) ^a	λ_{abs} (nm)	app. log K_{Fe}	app. BauB K_d (nM) ^c
Acb (Acb-Fe)	2:1 ^b	255, 330, 570 ^b	26.2 ± 0.1 ^b	300 ± 100 (160 ± 80) ^b
Fim (Fim-Fe)	1:1 ^b	255, 335, 445, 510 ^b	28.2 ± 0.2 ^b	360 ± 140 (240 ± 90) ^b
1 (1-Fe)	1:1 ^b	320, 455, 510	27.9 ± 0.1	390 ± 60 (350 ± 140)
2 (2-Fe)	1:1	320, 455, 510	28.2 ± 0.2	260 ± 60 (220 ± 30)
3 (3-Fe)	1:1	325, 455, 510	27.1 ± 0.2	240 ± 100 (290 ± 110)

^aSiderophore:Fe stoichiometry was measured by titration of siderophores with Fe(acac)₃ monitored by measuring fluorescence and/or optical absorbance. ^bLiterature values reported previously by our group.^{41,44,55} ^cValues in parentheses are for the ferric *holo*-siderophore complexes. Data is reported as mean ± standard deviation from the mean for at least two independent trials. All values were determined experimentally at a working pH of 7.4.

collected from the EDTA competition studies, we calculated apparent log K_{Fe} values of 27.9 ± 0.1, 28.2 ± 0.1, and 27.1 ± 0.1 for siderophores **1-Fe**, **2-Fe**, and **3-Fe**, respectively. While the *N*-acetyl derivative **2-Fe** did show slightly improved thermodynamic stability, the results indicate that the relative stability of the ferric iron chelation complexes is insensitive to functionalization of the *N*-acyl-hydroxamate moiety. The apparent log K_{Fe} values for **1-Fe**, **2-Fe**, and **3-Fe** are comparable to the reported values for **Acb-Fe** (26.2 ± 0.1) and **Fim-Fe** (28.2 ± 0.1), indicating that these siderophore analogues will be able to thermodynamically compete with native *A. baumannii* siderophores, most importantly with **Acb** the most critical virulence factor, in the sequestration of ferric iron under physiological conditions.^{41,44} It is noteworthy that compounds **1-Fe** and **3-Fe**, both of which can freely form salts with the free carboxyl and amino groups, respectively, are more soluble in buffered aqueous media than acetylated compound **2-Fe**.

BauB Receptor Binding to Mixed Ligand Siderophores. The ability of outer membrane receptors (OMRs) and periplasmic siderophore-binding proteins (SBPs) to recognize siderophore ligands through high-affinity reversible binding interactions is critical for siderophore import and function.⁷ *A. baumannii* pathogens strictly require the OMR BauA and SBP BauB for virulence associated with **Acb**-mediated iron acquisition.⁵³ BauA has been shown to recognize a novel mixed ferric iron chelation complex with one molecule of preacinetobactin bound to the receptor surface and one molecule of **Acb** exposed to solvent.⁵⁴ BauB displays broader ligand plasticity and binds to preacinetobactin, **Acb**, **Fim**, and analogues in both metal-free and ferric complex forms at nanomolar concentrations.^{17,41,55} **Acb** forms a 2:1 ligand:Fe(III) complex, referred to here as **Acb-Fe**, where the octahedral ferric iron atom forms coordinate bonds with

the phenolate-oxazoline and hydroxamate *N*-hydroxyl group of each molecule.⁵⁵ The crystal structure of **Acb-Fe** bound to the *A. baumannii* SBP BauB shows that residues in the binding calyx make hydrophobic interactions with the **Acb** ligand scaffold while the phenolate-oxazoline moiety of one **Acb** ligand is accommodated within a deep cleft; there are no direct interactions between BauB and the ferric iron center. This binding mode rationalizes the ability of BauB to accommodate both metal-free and metal bound siderophores. The biosynthetic operon for **Fim** does not include a dedicated periplasmic SBP.^{38,41} This is consistent with the hypothesis that **Fim** does not reach the cytoplasm of *A. baumannii*.¹¹ Our group used competition studies to show that **Fim-Fe** directly competes with **Acb-Fe** for binding to BauB.⁴¹ Although **Fim** forms a 1:1 ligand:Fe(III) complex, the structure of **Fim-Fe** is predicted to be similar to that of **Acb-Fe** where the shared phenolate-oxazoline moiety can occupy the same cleft in the BauB binding calyx.

If siderophores 1–3 are true structural mimics of **Fim**, we hypothesized that these molecules must be recognized by BauB through a high-affinity binding interaction. We tested this hypothesis using an intrinsic Trp fluorescence quenching binding assay with recombinant BauB protein (Table 1). We observed dose-dependent fluorescence quenching ($\lambda_{\text{excitation}} = 280$ nm; $\lambda_{\text{emission}} = 320$ nm) when titrating BauB with siderophores 1–3 and the corresponding ferric complexes, 1-Fe, 2-Fe, and 3-Fe (Figure S1). The apparent dissociation constants (K_d) were calculated using a one-site binding model according to the experimentally validated X-ray crystal structure of the 1:1 **Acb-Fe**:BauB complex (PDB 6mfl). The apparent K_d values for all three synthetic siderophore analogues were similar to the values measured for the natural siderophores, **Acb** and **Fim**, with all compounds falling within the range of 80–500 nM. **Acb** and **Fim** appeared to give lower apparent K_d values compared to compounds 1–3. Additionally, the ferric complexes all appeared to bind with greater affinity than the metal-free compounds; however, there was no significant difference when considering experimental error (Table 1). BauB binding to compounds 1–3 and the corresponding ferric complexes is not influenced significantly by the variable *N*-acyl-hydroxamate groups or electrostatics, indicating this might be a good position for attachment of linkers and antibiotics as done for the synthetic sideromycin 1-BL (Figure 1).^{11,28} The results from these SBP binding studies support the hypothesis that siderophores 1–3 are structural mimics of **Fim** and are consistent with previous observations that BauB and homologous periplasmic SBPs display broad ligand plasticity.

Mixed Ligand Siderophore Mimics Display Siderophore-like Activity. To further test the hypothesis that compounds 1–3 are recognized and utilized as siderophore substrates by *A. baumannii* pathogens, we performed growth promotion studies using *A. baumannii* ATCC 17978 under restricted iron conditions in M9-succinate minimal medium containing 2,2'-dipyridyl (Table 2; Figure 2). It is noteworthy that *A. baumannii* ATCC 17978 naturally produces and utilizes both **Acb** and **Fim**.⁴¹ We measured full bacterial growth curves by monitoring the optical density of cultures at 600 nm (OD_{600}) over a 48 h interval to evaluate the growth-stimulating effects of the siderophore compounds during all phases of growth (Figure S2). Comparison of the final OD_{600} values after 48 h revealed that in all cases the efficacy of ferric complexes outperformed the metal-free siderophores in promoting *A.*

Table 2. Apparent EC₅₀ and IC₅₀ Values for Siderophores and Mimics against Growth of *A. baumannii* ATCC 17978^a

cmpd	apparent EC ₅₀ (μM) ^b	apparent IC ₅₀ with Acb-Fe (μM)	apparent IC ₅₀ with FimA-Fe (μM)
Acb	30 ± 20	N/A ^c	N/A
Acb-Fe	0.6 ± 0.2	N/A	N/A
Fim	poor fit	N/A	N/A
Fim-Fe	0.2 ± 0.1	N/A	N/A
1	4 ± 1	N/A	N/A
1-Fe	1.4 ± 0.1	N/A	N/A
1-Ga	N/A	3 ± 1	50 ± 20
2	8 ± 3	N/A	N/A
2-Fe	0.9 ± 0.2	N/A	N/A
2-Ga	N/A	6 ± 1	40 ± 10
3	25 ± 9	N/A	N/A
3-Fe	1.2 ± 0.2	N/A	N/A
3-Ga	N/A	7 ± 1	30 ± 10

^aThe apparent EC₅₀ and IC₅₀ values were derived from OD₆₀₀ values at the 48 h time point (except for 1-Fe/2-Fe and 3-Fe taken at 37 and 31 h, respectively) collected during continuous analysis of growth curves. ^bApparent EC₅₀ values for **Acb**, **Acb-Fe**, **Fim**, and **Fim-Fe** were derived similarly from growth curves reported previously by our group.⁴¹ ^cN/A = not applicable. Data is reported as mean ± standard deviation for at least two independent trials.

baumannii growth (Figure 2a). Presumably the extra iron nutrient provided by the ferric complexes fueled greater cellular respiration and enable more biomass accumulation during the growth window. Comparison of the apparent EC₅₀ values of the compounds during the stationary phase of bacterial growth revealed that the ferric complexes have improved potency relative to metal-free compounds. The metal-free siderophores 1–3 produced a dose-dependent growth response with apparent EC₅₀ values comparable to the native siderophore **Acb**, all within the range of 3–50 μM covering both the low and high ends of the experimental error (Table 2; Figure 2B–F). The native siderophore **Fim** did not provide a sufficient dose response curve to calculate an apparent EC₅₀, which is consistent with previous reports that this compound becomes growth inhibitory at higher concentrations (also see bar graphs in Figure 2a for end-point analysis of bacterial growth where **Fim** supplementation does not recover growth above the control).⁴¹ The ferric complexes 1-Fe, 2-Fe, and 3-Fe produced apparent EC₅₀ values of potency comparable to that of **Acb-Fe** and **Fim-Fe**, all within the range of 0.1–1.5 μM covering both the low and high ends of the experimental error (Table 2; Figure 2B–F). The ability of siderophore analogues 1–3 and the corresponding ferric complexes to promote the growth of *A. baumannii* ATCC 17978 under restrictive iron conditions is not influenced significantly by electrostatics or sterics of the variable *N*-acyl-hydroxamate groups. This result is consistent with our findings for binding to the *A. baumannii* SBP BauB and further supports the conclusion that the *N*-acyl-hydroxamate group is a good site of functionalization to maintain siderophore-like activity of siderophore analogues.

Mixed Ligand Siderophore Mimics Compete with Native Siderophores for Cell Entry. The effective use of siderophore-based small molecules as antimicrobial agents hinges on the ability of these molecules to outcompete native siderophores utilized by the target pathogen that are readily available in the infection environment.⁵ To test the ability of siderophore analogues 1–3 to compete with native *A.*

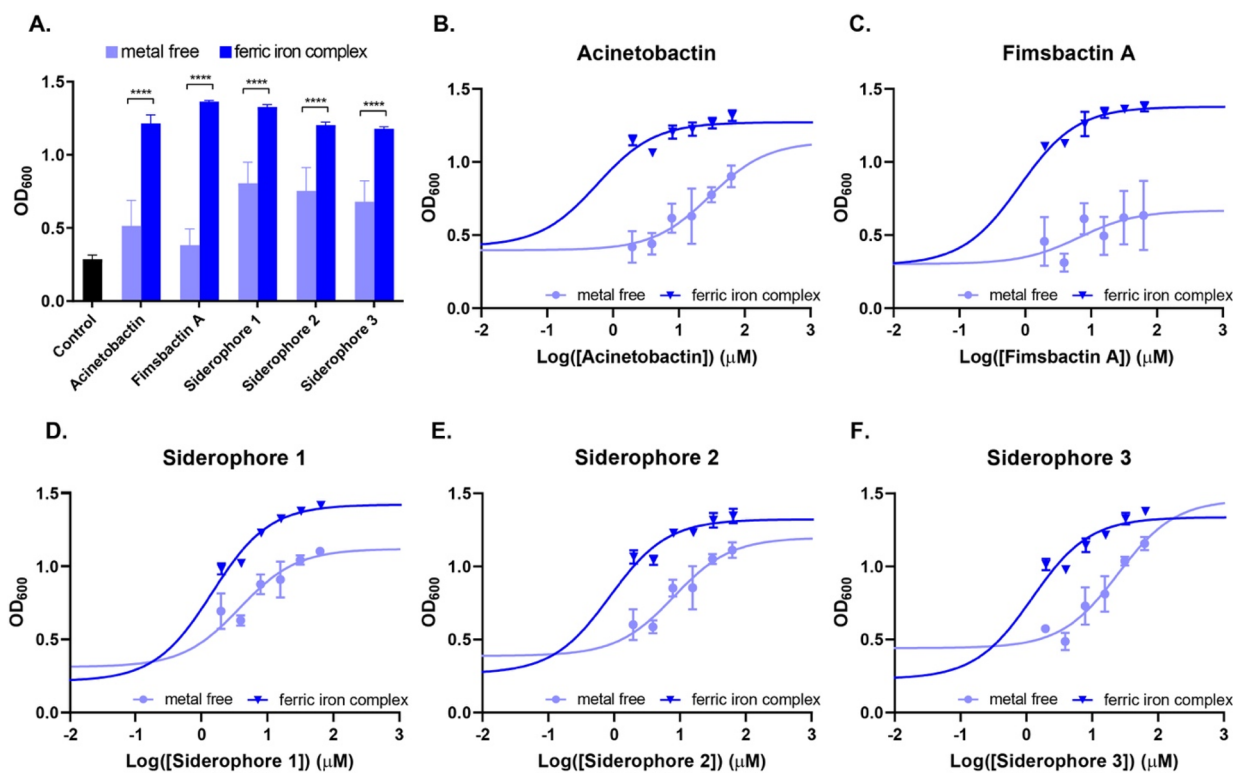


Figure 2. Mixed ligand siderophores 1–3 promote the growth of *A. baumannii* ATCC 17978 in iron-deficient M9-succinate minimal medium. (A) Bar graphs represent the mean OD₆₀₀ values measured after 40 h for each test compound at a final concentration of 15.6 μ M. (B–F) Apparent EC₅₀ curves for **Acb**, **Fim**, compounds 1–3 and the corresponding ferric complexes. See Table 1 and the experimental section for apparent EC₅₀ values and details on the source of OD₆₀₀ values used for EC₅₀ data plots. Error bars represent standard deviation for three independent biological replicates; **** $p < 0.0001$.

baumannii siderophores **Acb-Fe** and **Fim-Fe** for receptor-mediated uptake we performed competition studies with the Ga(III) complexes, **1-Ga**, **2-Ga**, and **3-Ga** (Table 2; Figures 3 and S3–S5). We first measured MIC₉₀ values for compounds **1-Ga**, **2-Ga**, and **3-Ga** alone against *A. baumannii* ATCC 17978 in M9-succinate minimal medium containing sufficient 2,2'-dipyridyl to create an iron-starved growth phenotype. Under these restrictive iron conditions, the Ga(III) siderophores complexes **1-Ga**, **2-Ga**, and **3-Ga** alone are potent growth inhibitors of *A. baumannii* ATCC 17978 with apparent MIC₉₀ values <1 μ M under the iron-restrictive M9 conditions. Redox stable Ga(III) salts can enter cells and metalate proteins and cofactors with Ga(III) instead of Fe(III)/Fe(II) through redox neutral ligand exchanges resulting in disruption of biological redox processes.¹² While we did not directly test this possibility for **1-Ga**, **2-Ga**, and **3-Ga**, we did investigate the possibility that these compounds can antagonize uptake and utilization of native siderophores under iron-restrictive growth conditions where these siderophores are essential growth factors. Given strain ATCC 17978 is a known producer of **Acb** and **Fim** in M9-succinate medium, we designed competitive studies to test the hypothesis that synthetic siderophores **1-Ga**, **2-Ga**, and **3-Ga** can outcompete native *A. baumannii* siderophores for cell entry and utilization.⁴¹

In some infection environments there might be an established titer of native siderophores that is not fully captured by the standard methods for MIC₉₀ determination *via* the broth microdilution assay where growth is initiated from a small number of cells in the inoculum.⁵⁶ Therefore, we performed direct competition studies using compounds **1-Ga**,

2-Ga, and **3-Ga** individually paired with either **Acb-Fe** or **Fim-Fe** supplemented to the growth medium. We used the apparent EC₅₀ values in Table 2 as a guide to select appropriate concentrations of **Acb-Fe** (3.9 μ M) and **Fim-Fe** (3.9 μ M) above the apparent EC₅₀ values to provide complete growth recovery of *A. baumannii* ATCC 17978 and represent a meaningful challenge for the synthetic siderophore Ga(III) complexes. Both **Acb-Fe** and **Fim-Fe** added to the M9 medium attenuated the growth inhibitory effects of **1-Ga**, **2-Ga**, and **3-Ga** (Table 2; Figure 3). Comparing “end point” OD₆₀₀ values after 48 h of bacterial growth in the presence of 31.25 μ M **1-Ga**, **2-Ga**, or **3-Ga** reveals that **Fim-Fe** more strongly antagonizes the growth inhibitory effects of the Ga(III) complexes compared to **Acb-Fe** (Figure 3). This trend is also captured by the apparent IC₅₀ values for **1-Ga**, **2-Ga**, and **3-Ga** ranging from 2 to 8 μ M in the presence of 3.9 μ M **Acb-Fe** and 20 to 70 μ M in the presence of 3.9 μ M **Fim-Fe** (both ranges account for the high and low ends of experimental error) (Table 2; Figure 3). These data are consistent with the hypothesis that siderophores 1–3 are synthetic mimics of **Fim**. Because **Fim** has been shown to outcompete **Acb** for cell entry,⁴¹ it follows that siderophores 1–3 and the corresponding Ga(III) complexes also outcompete **Acb**, as supported by these competition studies. Therefore, synthetic antimicrobial agents based on the common siderophore scaffold of compounds 1–3 are attractive because **Acb** is the only conserved and strictly required siderophore virulence factor for pathogenic *A. baumannii* strains.^{41,43,57}

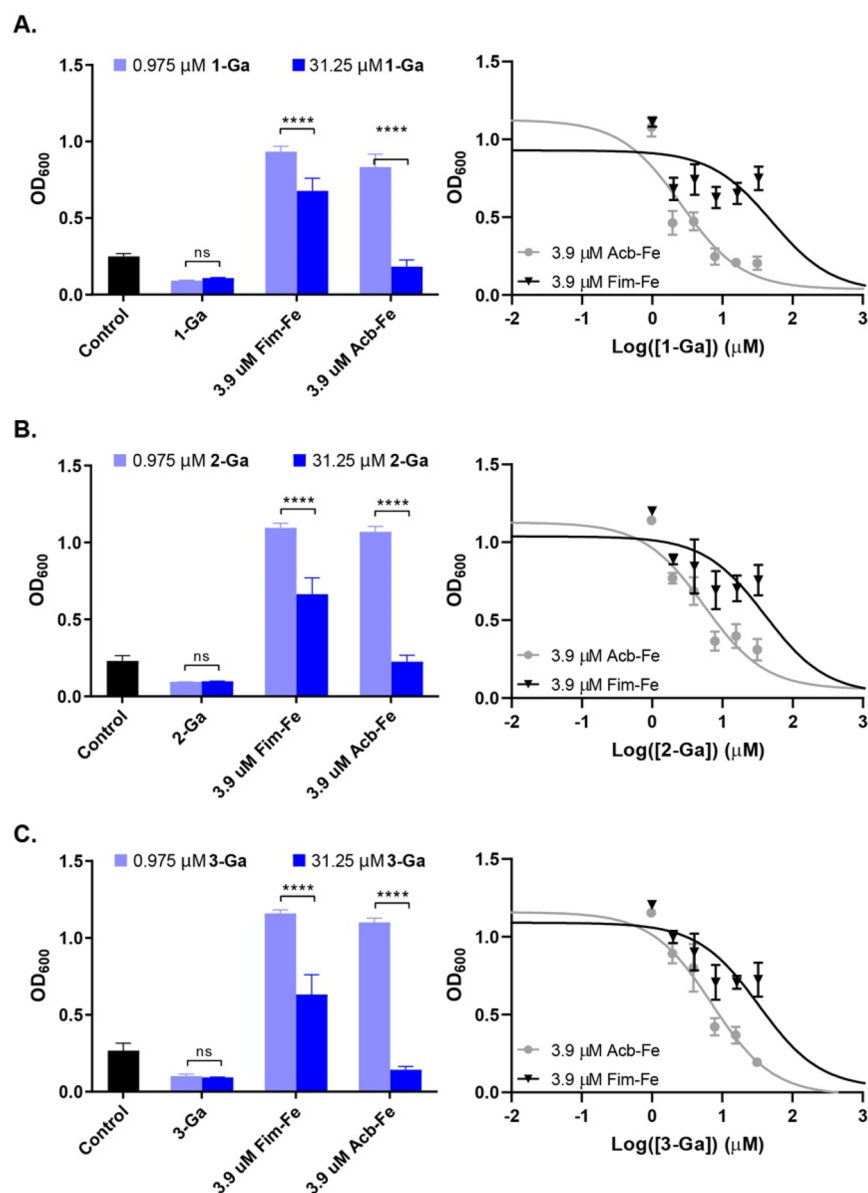


Figure 3. Gallium(III) complexes of mixed ligand siderophores 1–3 antagonize growth promotion of *A. baumannii* ATCC 17978 by native siderophores in iron-deficient M9-succinate minimal medium. Bar graphs represent the mean OD_{600} values measured after 48 h for representative low ($0.975 \mu\text{M}$) and high ($31.25 \mu\text{M}$) concentrations of (A) 1-Ga, (B) 2-Ga, and (C) 3-Ga in the presence of $3.9 \mu\text{M}$ Acb-Fe or Fim-Fe. IC_{50} curves are shown to highlight full dose-dependence of (A) 1-Ga, (B) 2-Ga, and (C) 3-Ga in the presence of $3.9 \mu\text{M}$ Acb-Fe or Fim-Fe. See Table 1 and the experimental section for apparent IC_{50} values and details on source of OD_{600} values used for IC_{50} data plots. Error bars represent standard deviation for three independent biological replicates; **** $p < 0.0001$.

There is a subtle, but potentially relevant, difference in the apparent IC_{50} values of analogues 1-Ga, 2-Ga, and 3-Ga in the presence of competing Fim-Fe. The apparent IC_{50} value of compound 1-Ga (50 ± 20) is greater than that of 3-Ga (30 ± 10) and 2-Ga (40 ± 10) (Table 2). While the confidence ranges are not statistically significant, ranking the apparent potency of these compounds as growth inhibitors based on the apparent mean IC_{50} values gives 3-Ga > 2-Ga > 1-Ga and suggests a potential trend of cationic > neutral > anionic for the *N*-acyl substituent of the hydroxamate group. The apparent differences in whole cell efficacies between 1-Ga, 2-Ga, and 3-Ga cannot be attributed to affinity for metal or receptor (Table 2) and must arise from other factors introduced by the *A. baumannii* cell. We observed a similar trend in electrostatics related to preferred siderophore utilization by *Staphylococcus*

aureus, but not receptor (FhuD2) or metal binding, for a series of synthetic ferrioxamine siderophores with variable *N*-acyl-hydroxamates.⁴⁷ For *S. aureus*, we hypothesized that the preference for cationic siderophores could be explained by simple electrostatics where the anionic cell envelope coated in anionic teichoic acid oligosaccharides repels anionic siderophores and attracts cationic siderophores. The same hypothesis applies to the *A. baumannii* cell envelope where the outer membrane coated in lipopolysaccharides carries a net negative charge. This implies that future applications of this synthetic mixed ligand siderophore scaffold for the development of siderophore-based antimicrobial agents targeting *A. baumannii* pathogens should be made to carry a cationic charge to promote greater intracellular accumulation. This general preference for cellular uptake of cationic compounds in

bacterial cells applies to most classes of organic molecules, including antibiotics.⁴

Ferric Complexes of Mixed Ligand Siderophores Mimic Fimbsactin. To date, X-ray crystal structures of *A. baumannii* siderophore-receptor complexes have been solved for **Acb-Fe** with the SBP BauB (PDB 6mfl) and a mixed preacinetobactin:**Acb** ferric complex with the OMR BauA (PDB 6h7f).^{54,55} In both structures, the binding calyx of BauB and BauA is occupied by only one ligand, **Acb** and preacinetobactin, respectively, in the $[\text{Fe}(\text{ligand})_2]$ complexes while the second ligand, **Acb** in both structures, is mostly solvent-exposed. We previously constructed a computational model of **Fim-Fe** using density functional theory (DFT) gas-phase calculations.⁴¹ Construction of this DFT model was informed by experimental data including the known coordination geometries and chelation modes of preacinetobactin and **Acb** from the BauA and BauB crystal structures, respectively. Additionally, we analyzed the optical absorbance spectra of **Acb-Fe**,⁴⁴ **Fim-Fe**,⁴¹ **1-Fe**, **2-Fe**, and **3-Fe** (Table 1; Figure S6). The absorbance spectrum of **Fim-Fe** shows strong absorbance bands at 255 and 335 nm that are consistent with similar absorbances at 284 and 336 nm in the absorbance spectrum of the vibriobactin, a tris-catecholate siderophore containing one catechol-oxazoline.⁴⁶ The absorbance bands at 284 and 335 nm in vibriobactin were experimentally correlated through pH titration to chelation of ferric iron through phenolate-oxazoline and catecholate chelation modes, respectively.⁵⁸ Thus, we assign the absorbance bands at 255 and 335 nm to the phenolate-oxazoline and catecholate chelation modes of **Fim-Fe**, respectively. This region of the absorbance spectra for compounds **1-Fe**, **2-Fe**, and **3-Fe** shows a strong absorbance at 320 nm corresponding to the catecholate chelation mode. Furthermore, comparing the ligand-to-metal charge-transfer bands for **Fim-Fe** (445, 510 nm) and compounds **1-Fe**, **2-Fe**, and **3-Fe** (455, 510 nm) suggests a similar ligand field effect around ferric iron. While we cannot rule out a salicylate binding mode for the synthetic siderophores,⁵⁹ for modeling purposes we investigated the bis-catecholate chelation mode of **2-Fe** with a high-spin ($S = 5/2$) octahedral ferric iron center.

Considering the above analyses, we used the DFT-modeled **Fim-Fe** structure (anionic $[\text{Fe}(\text{Fim})]^-$) as a starting point for DFT gas-phase calculations to model a high-spin ferric complex of synthetic siderophore **2-Fe** (anionic $[\text{Fe}(2)]^-$) (Figure 4). We aligned the *N*-acetyl-hydroxamate and two catecholates to match the analogous groups in the **Fim-Fe** DFT model. While **2-Fe** will form a racemic mixture, the enantiomer with stereochemical orientation matching the predicted biologically relevant enantiomer of **Fim-Fe** is shown. Our prediction of **Fim-Fe** stereochemistry is based on modeling to fit the BauB binding calyx.^{41,55} The stereochemistry of the **Fim-Fe** complex is predicted to be controlled, in part, by the orientation of the central *L*-Ser moiety.³⁸ Both DFT structures align well at the tetrahedral branching atom, the *L*-Ser α -carbon for **Fim-Fe** and the spermidine central nitrogen for **2-Fe**, where the tripodal branching “arms” can orient the metal chelating groups around the octahedral ferric iron center to minimize steric clashing and torsional strain. As shown in Figure 4, each branching “arm” is labeled by color and number to highlight similarities in the overall ligand orientation. Counting from the tetrahedral branching atom down branching “Arm 1”, the through-bond distance to the catechol hydroxyl groups in both compounds is

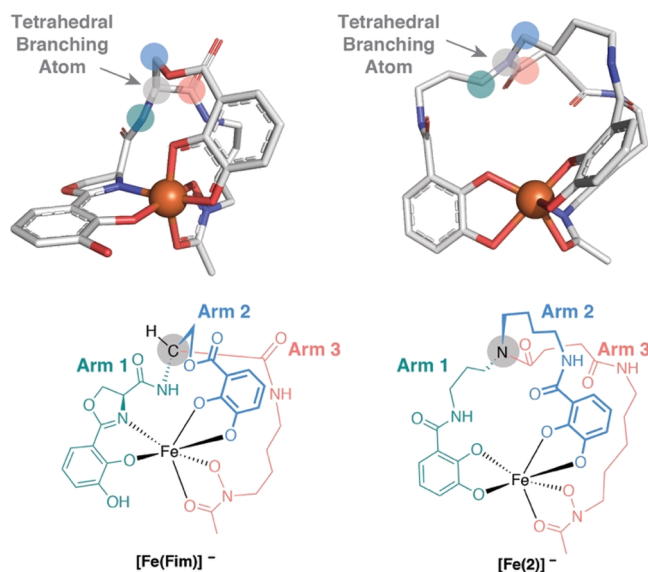


Figure 4. Comparison of monoanionic high-spin ($S = 5/2$) octahedral ferric iron complexes for naturally occurring **Fim-Fe** ($[\text{Fe}(\text{Fim})]^-$) and synthetic siderophore **2-Fe** ($[\text{Fe}(2)]^-$) generated using gas-phase DFT calculations.

the same; however, the oxazoline heterocycle restricts the flexibility of “Arm 1” in **Fim-Fe**, forcing the ligand into the phenolate-oxazoline chelation mode where the more flexible linkage in **2-Fe** facilitates the necessary geometry for chelation *via* the catecholate. In the case of vibriobactin, the phenolate-oxazoline chelation mode has been shown to be favored at neutral pH while the catecholate chelation mode can be populated at higher pH.⁵⁸ The same type of pH-dependent equilibrium of chelation modes is theoretically possible for **Fim-Fe**. The catecholate and hydroxamate ligands appended to “Arm 2” and “Arm 3”, respectively, are oriented similarly for both structures. Modeling of **Fim-Fe** to the crystal structure of the **Acb-Fe**:BauB complex suggests that the hydroxamate group will be solvent-exposed, supporting the observation that *N*-acyl-hydroxamate derivatives **1**, **2**, **3**, **1-BL**, and other reported conjugates linked *via* this position are well tolerated. Our modeling predicts that the *N*-acyl-hydroxamate is the most promising site for derivatization in the development of siderophore-based therapeutics based on synthetic siderophores **1–3** and derivatives thereof. Overall, the structure of **Fim-Fe** is more compact than that of **2-Fe** with calculated molecular surface areas of 1577 and 2125 Å², respectively. Incorporation of a catechol-oxazoline in place of the amide-linked catecholate might enable ferric iron chelation through the phenolate-oxazoline mode and improve likeness of the synthetic siderophores to naturally occurring **Fim-Fe**. Increasing structural likeness to **Fim** and **Fim-Fe** will presumably improve the ability of synthetic siderophore mimics to compete with the natural *A. baumannii* siderophores for cell entry under infection conditions.

CONCLUSIONS

Siderophore-based antibiotics hold much promise as future therapeutics for treating MDR Gram-negative infections. The siderophore component facilitates passage across the Gram-negative cell envelope overcoming the permeability barrier that defines the primary challenge of developing new antibiotics effective against Gram-negative pathogens. Approval of the first

siderophore-based antibiotic, cefiderocol, by the FDA in 2019 has brought renewed interest to the clinical viability of this therapeutic strategy to combat Gram-negative pathogens.⁶⁰ The ability of siderophore-based antibiotics to outcompete native siderophores for essential transporters is critical to lowering the risk of adaptive resistance by increasing the fitness cost of such adaptations.^{61,62} As demonstrated in this work, the careful and rational design of synthetic siderophore mimics of natural siderophores can expedite the development of siderophore-based therapeutics. Synthetic siderophores can be structurally tailored to match the native siderophore of a target pathogen and modified to allow for disruption of native siderophore trafficking, delivery of toxic metals, or targeting of traditional antibiotics. This form of siderophore subterfuge effectively tricks the target pathogen into “eating” a dietary supplement with no inherent nutritional value, thus starving the pathogen of the necessary iron nutrients needed for cellular metabolism. If the siderophore is “laced” with a toxic metal or antibiotic cargo, then consumption of the tainted siderophore “food” results in outright poisoning of the victim pathogen. Here, we have demonstrated that simply loading synthetic analogues of a native siderophore from *A. baumannii* with Ga(III) generates submicromolar growth inhibitory agents that outcompete native siderophores for receptor binding and cell entry. Spermidine-based fimsbactin mimics can be further adapted based on the design principles evaluated in this study to develop future siderophore-based therapeutic and diagnostic agents for *A. baumannii* pathogens.

METHODS

Strains, Materials, and Instrumentation. All solvents, chemicals, and reagents were purchased from Millipore Sigma, unless otherwise stated. Bacterial growth studies were conducted using *A. baumannii* ATCC 17978 in filter-sterilized M9 succinate minimal media containing 2,2'-dipyridyl to restrict available iron, as reported previously by our group.^{17,41,44,45} *E. coli* strains were grown in sterile Luria Broth (LB) for standard cultures and protein expression. Recombinant N-His₆-BauB was purified *via* Ni-NTA chromatography after expression from an *E. coli* BL21 heterologous host, as described previously.⁵⁵ Precultures and 96-well plate *A. baumannii* growth assays were performed in filter-sterilized M9 minimal medium prepared using polished water from a Milli-Q system. Fimsbactin A and acinetobactin were purified *via* prep-HPLC from cultures of *A. baumannii* ATCC 17978, as described previously.^{41,44} Samples for LC-MS were prepared in 0.45 μ M PTFE mini-UniPrep vials from Agilent. All prep-HPLC was performed using a Beckman Coulter SYSTEM GOLD 127P solvent module and 168 detector with a Phenomenex Luna 10u C18(2) 100A column, 250 \times 21.20 mm, 10 μ m with guard column. Prep-HPLC mobile phases were buffered with 5 mM ammonium acetate in (A) water and (B) acetonitrile, and data was processed using 32 Karat software, version 7.0. Low-resolution LC-MS was performed on an Agilent 6130 quadrupole LC-MS with G1313 autosampler, G1315 diode array detector, and 1200 series solvent module. A Phenomenex Gemini C18 column, 50 \times 2 mm, 5 μ m with guard column was used for all LC-MS separations. LC-MS mobile phases were 0.1% formic acid in (A) water and (B) acetonitrile, and data were processed using G2710 ChemStation software. NMR spectra were obtained on a Varian Unity Inova-600 MHz instrument with a cold probe. Bacterial growth studies were performed using sterile

polystyrene 96-well plates with polystyrene lids, and OD₆₀₀ measurements were obtained at 37 °C using a Molecular Devices SpectraMax Plus 384 plate reader. BauB binding studies were conducted using a fluorescence cuvette (HellmaAnalytics High Precision Cell cuvette made of Quartz SUPRASIL; light path 10 \times 2 mm), and emission spectra were recorded using a PerkinElmer LS 55 Luminescence Spectrometer (slit width 10 nm; scan speed 400 nm/min). Optical absorbance UV-vis spectra were obtained using a Cary 50 and disposable 1 cm methacrylate cuvettes.

Synthetic Protocols. The identity of known compounds was confirmed by ¹H NMR and LCMS analysis. All new compounds were fully characterized by ¹H NMR, ¹³C NMR, and high-res MS. Compound 13 (3.86 g, 3.62 mmol) was synthesized in 9 steps from commercially available 2,3-dihydroxybenzoic acid, 5-amino-1-pentanol, and spermidine using methods adapted from literature protocols reported by Wencewicz and Miller as shown in Scheme 1.^{11,23,28} Compound 13 was used as the universal precursor to our final siderophore targets for this study.

Compound 14. Compound 14 is a known compound previously synthesized by Wencewicz and Miller.^{11,28} Briefly, activated zinc (70 mg, 1.05 mmol) was added to a stirring solution of compound 13 (73 mg, 0.06 mmol) in a 1:1 mixture of THF:AcOH (10 mL total volume) at rt under an Ar atmosphere. Succinic anhydride (59 mg, 0.59 mmol) was added slowly as a solid. Reaction progress was monitored *via* LC-MS and was complete after \sim 3 h. The mixture was filtered to remove insoluble zinc salts, and the solvent was removed under reduced pressure using rotary evaporation. The resulting crude oil was dissolved in EtOAc and washed with water (2 \times) and brine (2 \times), dried over anhydrous magnesium sulfate, filtered, and concentrated under reduced pressure using rotary evaporation. The crude mixture was purified by prep-HPLC (C18-silica, 0% B to 95% B over 17 min, then 95% B to 100% B over 8 min) to afford compound 14 in 87% yield (60 mg, 0.06 mmol). ¹H NMR, ¹³C NMR, and LC-MS analyses were consistent with literature reports (Figures S7 and S8).^{11,28}

Compound 1. The first siderophore target, compound 1, is a known compound and was synthesized and characterized as previously reported.^{11,28} Briefly, to a stirring solution of compound 14 (73 mg, 0.06 mmol) dissolved in 1 mL of MeOH under an Ar atmosphere was added 10% Pd/C (10 mg) as a solid in one portion. The flask was purged with a balloon of H₂, and the resultant solution was stirred under an H₂ atmosphere (1 atm). Upon confirmation of reaction completion by LC-MS (\sim 1 h) the reaction mixture was filtered, and the solution was concentrated under reduced pressure *via* rotary evaporation. The resulting crude mixture was purified by prep-HPLC (C18-silica, 0% B to 95% B over 17 min, then 95% B to 100% B over 8 min) to afford compound 1 in 24% yield (10 mg, 0.01 mmol). ESI LC-MS, HR-MS and NMR analysis of 1 were consistent with previous reports.^{11,28} See Figures S9–S12 for characterization data and purity analysis (>95% by LC-MS).

Compound 15. Activated zinc (60 mg, 0.9 mmol) was added to a stirring solution of compound 13 (80 mg, 0.06 mmol) in a 1:1 mixture of THF:AcOH (10 mL total volume) at rt under an Ar atmosphere. Acetic anhydride (66 mg, 0.6 mmol) was added slowly with stirring. When the reaction was complete (as determined by LC-MS, \sim 3 h), the mixture was filtered to remove insoluble zinc salts, and the solvent was removed under reduced pressure using rotary evaporation. The

resultant crude oil was dissolved in EtOAc, washed with water (2×) and brine (2×), dried over anhydrous magnesium sulfate, filtered, and concentrated under reduced pressure using rotary evaporation. The crude mixture was purified by prep-HPLC (C18-silica, 0% B to 95% B over 17 min, then 95% B to 100% B over 8 min) to afford compound **15** in 84% yield (60 mg, 0.05 mmol). ¹H NMR (600 MHz, CDCl₃): δ 8.06–7.53 (m, 5H), 7.42–7.27 (m, 12H), 7.26–6.99 (m, 13H), 5.11–4.97 (m, 10H), 4.71 (d, *J* = 6.5 Hz, 2H), 3.72–3.64 (m, 1H), 3.59–3.48 (m, 2H), 3.24–2.99 (m, 11H), 2.58–2.35 (m, 5H), 2.01 (s, 3H), 1.50 (m, 4H), 1.43–1.26 (m, 2H). C NMR (150 MHz, CDCl₃): δ 177.46, 173.23, 172.72, 172.32, 171.24, 165.68, 165.47, 151.67, 146.81, 146.70, 136.34, 134.29, 129.16, 128.99, 128.77, 128.74, 128.69, 128.60, 128.28, 128.23, 127.63, 127.51, 126.98, 126.88, 124.45, 124.36, 123.19, 123.17, 123.07, 123.00, 117.09, 98.95, 71.27, 68.90, 67.93, 60.42, 53.44, 47.50, 45.51, 45.45, 44.92, 43.49, 39.45, 39.13, 38.98, 37.18, 37.09, 31.92, 31.57, 29.71, 29.36, 29.04, 28.78, 28.71, 28.50, 27.47, 26.58, 26.38, 25.91, 25.58, 25.26, 24.76, 23.77, 22.68, 22.16, 21.65, 21.04, 20.36, 18.75, 14.18, 14.11, 11.42. See Figures S13 and S14 for characterization data.

Compound 2. To a stirring solution of compound **15** (60 mg, 0.05 mmol) dissolved in 2 mL of MeOH under an Ar atmosphere was added 10% Pd/C (10 mg) as a solid in one portion. The flask was purged with a balloon of H₂, and the resultant solution was stirred under an H₂ atmosphere (1 atm). Upon confirmation of reaction completion by LC-MS (~1 h) the reaction mixture was filtered, and the solution was concentrated under reduced pressure using rotary evaporation. The resulting crude mixture was purified by prep-HPLC (C18-silica, 0% B to 95% B over 17 min, then 95% B to 100% B over 8 min) to afford compound **2** in 24% yield (8.6 mg, 0.01 mmol). ¹H NMR (600 MHz, CD₃OD): δ 7.25–7.18 (m, 2H), 6.95–6.89 (m, 2H), 6.75–6.66 (m, 2H), 3.50–3.43 (m, 6H), 3.13 (d, *J* = 6.8 Hz, 2H), 2.68 (dt, *J* = 18.4, 6.6 Hz, 2H), 2.54–2.45 (m, 2H), 1.98 (q, *J* = 8.0, 7.5 Hz, 1H), 1.93 (s, 3H), 1.86–1.79 (m, 2H), 1.76–1.57 (m, 6H), 1.51–1.43 (m, 4H). C NMR (150 MHz, CD₃OD): δ 173.34, 172.46, 171.77, 170.17, 148.88, 145.95, 118.15, 117.17, 115.33, 48.42, 45.27, 42.91, 38.93, 38.86, 38.60, 38.39, 36.55, 36.07, 32.66, 31.38, 30.53, 28.60, 28.52, 27.86, 27.04, 26.25, 25.58, 24.61, 23.80, 23.48, 22.67, 22.20, 21.12, 18.79. HR-MS (*m/z*): [M + H]⁺ calcd. C₃₂H₄₅N₅O₁₀: 660.3166, found 660.3234. See Figures S15–S18 for characterization data and purity analysis (>95% by LC-MS).

Compound 16. Activated zinc (60 mg, 0.9 mmol) was added to a stirring solution of compound **13** (44 mg, 0.04 mmol) in a 1:1 mixture of THF:AcOH (10 mL total volume) at rt under an Ar atmosphere. Cbz-beta-alanine-*N*-hydroxysuccinimide ester (113 mg, 0.35 mmol) was added to the mixture slowly. Upon reaction completion (as determined by LC-MS, ~3 h) the mixture was filtered to remove insoluble zinc salts and the solvent removed under reduced pressure using rotary evaporation. The resultant crude oil was dissolved in EtOAc, washed with water (2×) and brine (2×), dried over anhydrous magnesium sulfate, filtered, and concentrated under reduced pressure using rotary evaporation. The crude mixture was purified by prep-HPLC (C18-silica, 0% B to 95% B over 17 min, then 95% B to 100% B over 8 min) to afford compound **16** in 19% yield (10 mg, 0.008 mmol). ¹H NMR (600 MHz, CDCl₃): δ 8.09–7.88 (m, 3H), 7.75–7.59 (m, 2H), 7.48–7.28 (m, 30H), 7.19–7.06 (m, 4H), 5.18–5.02 (m, 12H), 4.73 (d, *J* = 6.7 Hz, 2H), 3.29–3.03 (m, 11H), 2.60 (d, *J*

= 6.2 Hz, 2H), 2.54–2.36 (m, 5H), 1.64–1.31 (m, 8H). C NMR (150 MHz, CDCl₃): δ 173.36, 172.54, 171.85, 171.54, 165.46, 165.24, 162.38, 156.41, 151.68, 146.79, 146.62, 136.58, 136.37, 134.14, 129.22, 129.03, 128.75, 128.69, 128.55, 128.52, 128.45, 128.28, 128.21, 128.01, 127.99, 127.65, 127.63, 127.11, 124.43, 124.34, 123.22, 123.14, 122.98, 117.11, 116.99, 116.86, 116.73, 76.46, 76.38, 76.24, 71.28, 71.19, 66.49, 47.33, 45.54, 45.38, 45.05, 43.31, 39.30, 39.23, 38.99, 37.08, 36.39, 32.56, 31.64, 29.70, 28.93, 28.71, 28.64, 27.53, 26.74, 26.65, 26.45, 26.01, 24.98, 23.89, 22.69. See Figures S19 and S20 for characterization data.

Compound 3. To a stirring solution of compound **16** (10 mg, 0.008 mmol) dissolved in 1 mL MeOH under an Ar atmosphere was added 10% Pd/C (10 mg) as a solid. The flask was purged with a balloon of H₂, and the resultant solution stirred under an H₂ atmosphere (1 atm). Upon confirmation of reaction completion by LC-MS (~1 h) the reaction mixture was filtered, and the solution was concentrated under reduced pressure *via* rotary evaporation. The resulting crude mixture was purified by prep-HPLC (C18-silica, 0% B to 95% B over 17 min, then 95% B to 100% B over 8 min) to afford compound **3** in 78% yield (4.2 mg, 0.006 mmol). ¹H NMR (600 MHz, DMSO): δ 7.42–6.56 (m, 6H), 3.38–3.09 (m, 3H), 3.06–2.90 (m, 3H), 2.72–2.64 (m, 1H), 2.42–2.16 (m, 2H), 2.03–1.63 (m, 1H), 1.60–1.10 (m, 16H). C NMR (150 MHz, DMSO): δ 173.21, 171.71, 163.80, 156.46, 150.05, 146.68, 137.60, 128.80, 128.17, 119.17, 118.53, 118.07, 117.52, 115.36, 65.65, 52.25, 51.81, 38.87, 36.98, 34.62, 32.91, 31.55, 30.99, 29.48, 29.24, 26.63, 25.27, 24.16, 23.24, 22.48, 17.28, 14.45, 12.81. HR-MS (*m/z*): [M + H]⁺ calcd. C₃₃H₄₈N₆O₁₀: 689.3432, found 689.3957. See Figures S21–S24 for characterization data and purity analysis (>90% by LC-MS).

Preparation of Fe(III) and Ga(III) Siderophore Complexes. The Fe(III) complexes of **Fim**, **Acb**, and compounds **1–3** were prepared by treatment with Fe(acac)₃ in MeOH, respectively. Samples were concentrated under reduced pressure using rotary evaporation, and the resulting residue was triturated with Et₂O to remove excess acac ligand. Stoichiometric Fe(acac)₃ was used to prepare 1:1 metal:ligand complexes with **Fim** and compounds **1–3**.^{11,41} We refer to these metal complexes as **Fim-Fe**, **1-Fe**, **2-Fe**, and **3-Fe**. A 2:1 ratio of **Acb**:Fe(acac)₃ was used to form the corresponding [Fe(**Acb**)₂] complex, referred to simply as **Acb-Fe**. The Ga(III) complexes of compounds **1–3** (**1-Ga**, **2-Ga**, and **3-Ga**) were prepared analogously using stoichiometric Ga(acac)₃. All siderophore metal chelation complexes were prepared fresh directly before biological or biochemical studies.

A. baumannii Growth Studies with Metal-free Siderophores and Ferric Iron Complexes. Stock solutions of each test compound (**1**, **1-Fe**, **2**, **2-Fe**, **3**, and **3-Fe**) were prepared in DMSO at a concentration of 10 mM. A 96-well plate was filled with 50 μL of M9-succinate minimal medium per well. The DMSO stock solutions were diluted in sterile M9-succinate minimal medium providing a working concentration of 250 μM test compound. A 50 μL aliquot of this M9-succinate solution was added to the first row of a 96-well plate preloaded with 50 μL of sterile M9-succinate medium in each well. Each test compound was serially diluted 2-fold down the row of each 96-well plate. An inoculum was made by adding 100 μL of 0.5 McFarland standard of *A. baumannii* ATCC 17978 prepared from a fresh overnight culture to 4.0 mL of sterile M9-succinate minimal media supplemented with 350 μM 2,2'-dipyridyl. Plates were inoculated by adding 50 μL of

inoculum to each well giving a final total volume of 100 μL per well containing a final concentration of 175 μM 2,2'-dipyridyl and a concentration range of 1.95–62.5 μM test compound. OD₆₀₀ measurements were recorded at 37 °C to generate growth curves over a 48 h window (Figure S2). All experiments were performed in triplicate as independent trials. Growth curves for *A. baumannii* ATCC 17978 treated with **Fim**, **Fim-Fe**, **Acb**, and **Acb-Fe** were reported previously by our group.⁴¹ EC₅₀ values were determined by plotting OD₆₀₀ values at the 48 h (**Acb**, **Fim**, 1–3, **Acb-Fe**, and **Fim-Fe**), 37 h (**1-Fe** and **2-Fe**), or 31 h (**3-Fe**) time point versus the log value of the test compound concentration in GraphPad Prism v7.0b. The leftmost anchor point (not shown) is the OD₆₀₀ value derived from the control growth curves containing no added siderophores (Figure S2).

A. baumannii Growth Studies with Ga(III) Complexes. Stock solutions of each test compound (**Fim-Fe**, **Acb-Fe**, **1-Ga**, **2-Ga**, and **3-Ga**) were prepared in DMSO at a concentration of 10 mM. A 96-well plate was filled with 50 μL of M9-succinate minimal medium per well. The DMSO stock solutions were diluted in M9-succinate minimal medium providing a working concentration of 125 μM test compound. A 50 μL aliquot of this M9-succinate solution was added to the first row of a 96 well plate preloaded with 50 μL of sterile M9-succinate medium in each well. Each test compound was serially diluted 2-fold down the row of each 96-well plate. An inoculum was made by adding 100 μL of 0.5 McFarland standard of *A. baumannii* ATCC 17978 prepared from a fresh overnight culture to 4.0 mL of sterile M9-succinate minimal media supplemented with 350 μM 2,2'-dipyridyl. Plates were inoculated by adding 50 μL of inoculum to each well, giving a final total volume of 100 μL per well containing a final concentration of 175 μM 2,2'-dipyridyl and a concentration range of 0.975–31.25 μM test compound. Wells were then spiked with 2 μL of either M9-succinate medium (control), **Acb-Fe** (195 μM stock in M9), or **Fim-Fe** (195 μM stock in M9) resulting in final concentrations of **Acb-Fe** or **Fim-Fe** of 3.9 μM in test wells to create a competition scenario with **1-Ga**, **2-Ga**, or **3-Ga**. OD₆₀₀ measurements were recorded at 37 °C to generate growth curves over a 48 h window (Figures S3–S5). All experiments were performed in triplicate as independent trials. IC₅₀ values were determined by plotting OD₆₀₀ values at the 40 h time point versus the log value of the test compound concentration in GraphPad Prism v7.0b. The leftmost anchor point (not shown) was generated from OD₆₀₀ values of control growth curves in the presence of 3.9 μM **Acb-Fe** or 3.9 μM **Fim-Fe** and no **1-Ga**, **2-Ga**, or **3-Ga**. The rightmost anchor point (not shown) was generated from OD₆₀₀ values of control growth curves with no added **Acb-Fe**, **Fim-Fe**; or **1-Ga**, **2-Ga**, or **3-Ga** (Figures S3–S5).

BauB Binding Studies. BauB fluorescence quenching studies were performed as previously reported using a soluble truncated *N*-His₆-tagged protein construct.^{41,55} Briefly, a bead of purified recombinant *N*-His₆-BauB was thawed and diluted in assay buffer (25 mM Tris-HCl, 8 g/L NaCl, 0.2 g/L KCl, pH 7.4) to provide a 400 nM BauB stock solution. A 300 μL portion of this 400 nM BauB stock solution was transferred to a fluorescence cuvette in the presence of variable ligand (**1–3**, **1-Fe**, **2-Fe**, or **3-Fe**) concentrations (0, 106.8, 212.8, 318, 422.4, 684, 1196, 1688, 2644, and 3536 nM). An emission spectrum ($\lambda_{\text{emission}} = 300\text{--}400$ nm) was recorded at each concentration as an average of 3 scans using $\lambda_{\text{excitation}} = 280$ nm. All measurements were performed in duplicate as independent

trials. Fluorescence intensity at 320 nm was plotted versus substrate concentration (nM), and apparent K_d was calculated using nonlinear regression analysis and a single binding site model in GraphPad Prism v7.0b (Figure S1). All experiments were performed in triplicate as independent trials.

Ferric Iron Binding Studies. A competition assay with EDTA was used to determine the apparent K_{Fe} of siderophores **1–3** for ferric iron. Stock solutions of siderophore ferric iron complexes, **1-Fe**, **2-Fe**, and **3-Fe**, were prepared in HEPES buffer (10 mM HEPES, 600 mM NaCl, 100 mM KCl, pH 7.4) at 100 μM . An optical absorbance spectrum of each compound was obtained from $\lambda = 300\text{--}800$ nm (Figure S6). EDTA was added to each compound solution giving a final concentration of 120 μM , a 20% excess relative to each test compound. Optical absorbance was monitored continuously at 500 nm for up to 800 min or until equilibrium was reached. The apparent K_{Fe} values were calculated using the total change in optical absorbance at 500 nm using equations previously reported by our group.⁴¹ We assumed a K_{Fe} value of $10^{25.1}$ for EDTA-Fe at pH 7.4 when calculating apparent K_{Fe} values.⁵² All experiments were performed in triplicate as independent trials.

DFT Calculations. Relative thermodynamic stabilities for ferric siderophore complexes **Fim-Fe** and **2-Fe** were calculated using density functional theory (DFT) in the gas phase following a protocol previously reported by our group.^{41,55} We previously optimized a model structure for **Fim-Fe** using the monoanionic $[\text{Fe}(\text{Fim})]^-$ high-spin ($S = 5/2$) ferric complex modeled against a crystal structure of monoanionic $[\text{Fe}(\text{Acb})_2]^-$ bound to the siderophore-binding protein BauB (PDB 6fml) as starting geometry. Here, we modeled the high-spin monoanionic $[\text{Fe}(2)]^-$ using an analogous workflow. Molecular surface area was calculated using the functional built into PyMOL v2.3.2 (Schrodinger LLC). 3D renderings of molecules were generated using this same software.

■ ASSOCIATED CONTENT

Supporting Information

The Supporting Information is available free of charge at <https://pubs.acs.org/doi/10.1021/acsinfectdis.1c00119>.

Supporting figures, supporting tables, compound characterization data, compound purity analysis, high-resolution mass spectra, LC-MS chromatograms, NMR spectra, optical absorbance spectra, *A. baumannii* growth curves, and BauB fluorescence quenching plots (PDF)

■ AUTHOR INFORMATION

Corresponding Author

Timothy A. Wencewicz – Department of Chemistry, Washington University in St. Louis, St. Louis, Missouri 63130, United States; orcid.org/0000-0002-5839-6672; Phone: 314-935-7247; Email: wencewicz@wustl.edu; Fax: 314-935-4481

Authors

Tabbetta J. Bohac – Department of Chemistry, Washington University in St. Louis, St. Louis, Missouri 63130, United States

Luting Fang – Department of Chemistry, Washington University in St. Louis, St. Louis, Missouri 63130, United States

Victoria S. Banas – Department of Chemistry, Washington University in St. Louis, St. Louis, Missouri 63130, United States

Daryl E. Giblin – Department of Chemistry, Washington University in St. Louis, St. Louis, Missouri 63130, United States

Complete contact information is available at:

<https://pubs.acs.org/10.1021/acsinfecdis.1c00119>

Author Contributions

[§]T.J.B., L.F., and V.S.B. contributed equally to this work.

Notes

The authors declare no competing financial interest.

ACKNOWLEDGMENTS

We thank Dr. Brad Evans at the Proteomics & Mass Spectrometry Facility at the Donald Danforth Plant Science Center, St. Louis, MO for assistance with the acquisition of the QTRAP LC-MS/MS spectra (supported by the National Science Foundation under Grant No. DBI-0521250). We thank Prof. John-Stephen Taylor (WUSTL, Dept. of Chemistry) for assistance with fluorescence quenching studies. We thank Prof. Andy Gulick and Dr. Daniel Bailey (State University of New York at Buffalo) for the pET28-TEV plasmid used for expression of BauB. We thank the National Science Foundation (NSF) for supporting this work through CAREER Award 1654611 to T.A.W.

ABBREVIATIONS

Acb, acinetobactin; Acb-Fe, acinetobactin ferric iron complex; ACN, acetonitrile; BME, β -mercaptoethanol; CP, cytoplasm; DFT, density functional theory; DTT, dithiothreitol; ESI, electrospray ionization; Fim, fimsbactin; Fim-Fe, fimsbactin ferric iron complex; His₆, hexahistidine; HPLC, high-performance liquid chromatography; IM, inner membrane; im, imidazole; LB, Luria Broth; LC-MS, liquid chromatography–mass spectrometry; MWCO, molecular weight cutoff; Ni-NTA, nickel nitrilotriacetic acid agarose; OM, outer membrane; OMR, outer membrane receptor; PAGE, polyacrylamide gel electrophoresis; PDB, protein data bank; rpm, rotations per minute; rt, room temperature; SBP, siderophore-binding protein; SDS, sodium dodecyl sulfate

REFERENCES

- (1) Antibiotic resistance threats in the United States, 2019; Center for Disease Control and Prevention, U.S. Department of Health and Human Services; Washington, DC, Published Online Nov. 13, 2019.
- (2) Morris, S., and Cerceo, E. (2020) Trends, Epidemiology, and Management of Multi-Drug Resistant Gram-Negative Bacterial Infections in the Hospitalized Setting. *Antibiotics* 9, 196.
- (3) Imai, Y., Meyer, K. J., Iinishi, A., Favre-Godal, Q., Green, R., Manuse, S., Caboni, M., Mori, M., Niles, S., Ghiglieri, M., Honrao, C., Ma, X., Guo, J. J., Makriyannis, A., Linares-Otaya, L., Böhringer, N., Wuisan, Z. G., Kaur, H., Wu, R., Mateus, A., Typas, A., Savitski, M. M., Espinoza, J. L., O'Rourke, A., Nelson, K. E., Hiller, S., Noinaj, N., Schäberle, T. F., D'Onofrio, A., and Lewis, K. (2019) A New Antibiotic Selectively Kills Gram-Negative Pathogens. *Nature* 576, 459–464.
- (4) Richter, M. F., Drown, B. S., Riley, A. P., Garcia, A., Shirai, T., Svec, R. L., and Hergenrother, P. J. (2017) Predictive Compound Accumulation Rules Yield a Broad-Spectrum Antibiotic. *Nature* 545, 299–304.
- (5) Wenciewicz, T. A., and Miller, M. J. (2018) Sideromycins as Pathogen-Targeted Antibiotics. In *Antibacterials: Vol. II* (Fisher, J. F.,

Mobashery, S., and Miller, M. J., Eds.), pp 151–183, Springer International Publishing, Cham. DOI: 10.1007/7355_2017_19.

(6) Neilands, J. B. (1995) Siderophores: Structure and Function of Microbial Iron Transport Compounds. *J. Biol. Chem.* 270, 26723–26726.

(7) Hider, R. C., and Kong, X. (2010) Chemistry and Biology of Siderophores. *Nat. Prod. Rep.* 27, 637–657.

(8) Endicott, N. P., Rivera, G. S. M., Yang, J., and Wenciewicz, T. A. (2020) Emergence of Ferrichelatase Activity in a Siderophore-Binding Protein Supports an Iron Shuttle in Bacteria. *ACS Cent. Sci.* 6, 493–506.

(9) Miethke, M., and Marahiel, M. A. (2007) Siderophore-Based Iron Acquisition and Pathogen Control. *Microbiol. Mol. Biol. Rev.* 71, 413–451.

(10) Harding, C. M., Hennon, S. W., and Feldman, M. F. (2018) Uncovering the Mechanisms of *Acinetobacter baumannii* Virulence. *Nat. Rev. Microbiol.* 16, 91–102.

(11) Wenciewicz, T. A., and Miller, M. J. (2013) Biscatecholate-Monohydroxamate Mixed Ligand Siderophore-Carbacephalosporin Conjugates are Selective Sideromycin Antibiotics that Target *Acinetobacter baumannii*. *J. Med. Chem.* 56, 4044–4052.

(12) Banin, E., Lozinski, A., Brady, K. M., Berenshtein, E., Butterfield, P. W., Moshe, M., Chevion, M., Greenberg, E. P., and Banin, E. (2008) The Potential of Desferrioxamine-Gallium as an anti-*Pseudomonas* Therapeutic Agent. *Proc. Natl. Acad. Sci. U. S. A.* 105, 16761–16766.

(13) Pandey, A., Savino, C., Ahn, S. H., Yang, Z., Van Lanen, S. G., and Boros, E. (2019) Theranostic Gallium Siderophore Ciprofloxacin Conjugate with Broad Spectrum Antibiotic Potency. *J. Med. Chem.* 62, 9947–9960.

(14) Drake, E. J., Duckworth, B. P., Neres, J., Aldrich, C. C., and Gulick, A. M. (2010) Biochemical and Structural Characterization of Bisubstrate Inhibitors of BasE, the Self-Standing Nonribosomal Peptide Synthetase Adenylate-Forming Enzyme of *Acinetobacter* Synthesis. *Biochemistry* 49, 9292–9305.

(15) Wurst, J. M., Drake, E. J., Theriault, J. R., Jewett, I. T., VerPlank, L., Perez, J. R., Dandapani, S., Palmer, M., Moskowitz, S. M., Schreiber, S. L., Munoz, B., and Gulick, A. M. (2014) Identification of Inhibitors of PvdQ, an Enzyme Involved in the Synthesis of the Siderophore Pyoverdine. *ACS Chem. Biol.* 9, 1536–1544.

(16) Tripathi, A., Schofield, M. M., Chlipala, G. E., Schultz, P. J., Yim, I., Newmister, S. A., Nusca, T. D., Scaglione, J. B., Hanna, P. C., Tamayo-Castillo, G., and Sherman, D. H. (2014) Baulamycins A and B, Broad-Spectrum Antibiotics Identified as Inhibitors of Siderophore Biosynthesis in *Staphylococcus aureus* and *Bacillus anthracis*. *J. Am. Chem. Soc.* 136, 1579–1586.

(17) Bohac, T. J., Shapiro, J. A., and Wenciewicz, T. A. (2017) Rigid Oxazole Acinetobactin Analog Blocks Siderophore Cycling in *Acinetobacter baumannii*. *ACS Infect. Dis.* 3, 802–806.

(18) Yep, A., McQuade, T., Kirchhoff, P., Larsen, M., and Mobley, H. L. T. (2014) Inhibitors of TonB Function Identified by a High-Throughput Screen for Inhibitors of Iron Acquisition in Uropathogenic *Escherichia coli* CFT073. *mBio* 5, e01089–13.

(19) Nairn, B. L., Eliasson, O. S., Hyder, D. R., Long, N. J., Majumdar, A., Chakravorty, S., McDonald, P., Roy, A., Newton, S. M., and Klebba, P. E. (2017) Fluorescence High-Throughput Screening for Inhibitors of TonB Action. *J. Bacteriol.* 199, e00889-16 DOI: 10.1128/JB.00889-16.

(20) Hennard, C., Truong, Q. C., Desnottes, J. F., Paris, J. M., Moreau, N. J., and Abdallah, M. A. (2001) Synthesis and Activities of Pyoverdine-Quinolone Adducts: A Prospective Approach to a Specific Therapy Against *Pseudomonas aeruginosa*. *J. Med. Chem.* 44, 2139–2151.

(21) Miller, M. J., Walz, A. J., Zhu, H., Wu, C., Moraski, G., Möllmann, U., Tristani, E. M., Crumbliss, A. L., Ferdig, M. T., Checkley, L., Edwards, R. L., and Boshoff, H. I. (2011) Design, Synthesis, and Study of a Mycobactin-Artemisinin Conjugate that has

- Selective and Potent Activity Against Tuberculosis and Malaria. *J. Am. Chem. Soc.* 133, 2076–2079.
- (22) Zheng, T., and Nolan, E. M. (2014) Enterobactin-Mediated Delivery of β -Lactam Antibiotics Enhances Antibacterial Activity Against Pathogenic *Escherichia coli*. *J. Am. Chem. Soc.* 136, 9677–9691.
- (23) Ghosh, A., Ghosh, M., Niu, C., Malouin, F., Moellmann, U., and Miller, M. J. (1996) Iron Transport-Mediated Drug Delivery Using Mixed-Ligand Siderophore-beta-Lactam Conjugates. *Chem. Biol.* 3, 1011–1019.
- (24) Betoudji, F., Abd El Rahman, T., Miller, M. J., Ghosh, M., Jacques, M., Bouarab, K., and Malouin, F. (2020) A Siderophore Analog of Fimsbactin from *Acinetobacter* Hinders Growth of the Phytopathogen *Pseudomonas syringae* and Induces Systemic Priming of Immunity in *Arabidopsis thaliana*. *Pathogens* 9, 806.
- (25) Hu, J., Ghosh, M., Miller, M. J., and Bohn, P. W. (2019) Whole-Cell Biosensing by Siderophore-Based Molecular Recognition and Localized Surface Plasmon Resonance. *Anal. Methods* 11, 296–302.
- (26) Ghosh, M., Miller, P. A., Mollmann, U., Claypool, W. D., Schroeder, V. A., Wolter, W. R., Suckow, M., Yu, H., Li, S., Huang, W., Zajicek, J., and Miller, M. J. (2017) Targeted Antibiotic Delivery: Selective Siderophore Conjugation with Daptomycin Confers Potent Activity against Multidrug Resistant *Acinetobacter baumannii* Both in Vitro and in Vivo. *J. Med. Chem.* 60, 4577–4583.
- (27) Ghosh, M., Lin, Y. M., Miller, P. A., Mollmann, U., Boggess, W. C., and Miller, M. J. (2018) Siderophore Conjugates of Daptomycin are Potent Inhibitors of Carbapenem Resistant Strains of *Acinetobacter baumannii*. *ACS Infect. Dis.* 4, 1529–1535.
- (28) Ghosh, M., and Miller, M. J. (1996) Synthesis and In Vitro Antibacterial Activity of Spermidine-Based Mixed Catechol- and Hydroxamate-Containing Siderophore-Vancomycin Conjugates. *Bioorg. Med. Chem.* 4, 43–48.
- (29) Ghosh, M., Miller, P. A., and Miller, M. J. (2020) Antibiotic Repurposing: bis-Catechol- and Mixed Ligand (bis-Catechol-mono-Hydroxamate)-Teicoplanin Conjugates are Active Against Multidrug Resistant *Acinetobacter baumannii*. *J. Antibiot.* 73, 152–157.
- (30) Ji, C., and Miller, M. J. (2012) Chemical Syntheses and In Vitro Antibacterial Activity of Two Desferrioxamine B-Ciprofloxacin Conjugates with Potential Esterase and Phosphatase Triggered Drug Release Linkers. *Bioorg. Med. Chem.* 20, 3828–3836.
- (31) Ji, C., and Miller, M. J. (2015) Siderophore-Fluoroquinolone Conjugates Containing Potential Reduction-Triggered Linkers for Drug Release: Synthesis and Antibacterial Activity. *BioMetals* 28, 541–551.
- (32) Liu, R., Miller, P. A., Vakulenko, S. B., Stewart, N. K., Boggess, W. C., and Miller, M. J. (2018) A Synthetic Dual Drug Sideromycin Induces Gram-Negative Bacteria To Commit Suicide with a Gram-Positive Antibiotic. *J. Med. Chem.* 61, 3845–3854.
- (33) Zheng, T., and Nolan, E. M. (2015) Evaluation of (Acyloxy)alkyl Ester Linkers for Antibiotic Release From Siderophore-Antibiotic Conjugates. *Bioorg. Med. Chem. Lett.* 25, 4987–4991.
- (34) Neumann, W., Sassone-Corsi, M., Raffatelli, M., and Nolan, E. M. (2018) Esterase-Catalyzed Siderophore Hydrolysis Activates an Enterobactin-Ciprofloxacin Conjugate and Confers Targeted Antibacterial Activity. *J. Am. Chem. Soc.* 140, 5193–5201.
- (35) Neumann, W., and Nolan, E. M. (2018) Evaluation of a Reducible Disulfide Linker for Siderophore-Mediated Delivery of Antibiotics. *JBIC, J. Biol. Inorg. Chem.* 23, 1025–1036.
- (36) Boyce, J. H., Dang, B., Ary, B., Edmondson, Q., Craik, C. S., DeGrado, W. F., and Seiple, I. B. (2020) Platform to Discover Protease-Activated Antibiotics and Application to Siderophore-Antibiotic Conjugates. *J. Am. Chem. Soc.* 142, 21310–21321.
- (37) Wenciewicz, T. A., Möllmann, U., Long, T. E., and Miller, M. J. (2009) Is Drug Release Necessary for Antimicrobial Activity of Siderophore-Drug Conjugates? Syntheses and Biological Studies of the Naturally Occurring Salmycin "Trojan Horse" Antibiotics and Synthetic Desferrioxamine-Antibiotic Conjugates. *BioMetals* 22, 633–648.
- (38) Proschak, A., Lubuta, P., Grun, P., Lohr, F., Wilharm, G., De Berardinis, V., and Bode, H. B. (2013) Structure and Biosynthesis of Fimsbactins A-F, Siderophores from *Acinetobacter baumannii* and *Acinetobacter baylyi*. *ChemBioChem* 14, 633–638.
- (39) Yamamoto, S., Okujo, N., and Sakakibara, Y. (1994) Isolation and Structure Elucidation of Acinetobactin, a Novel Siderophore from *Acinetobacter baumannii*. *Arch. Microbiol.* 162, 249–254.
- (40) Penwell, W. F., DeGrace, N., Tentarelli, S., Gauthier, L., Gilbert, C. M., Arivett, B. A., Miller, A. A., Durand-Reville, T. F., Joubran, C., and Actis, L. A. (2015) Discovery and Characterization of New Hydroxamate Siderophores, Baumannoferrin A and B, produced by *Acinetobacter baumannii*. *ChemBioChem* 16, 1896–1904.
- (41) Bohac, T. J., Fang, L., Giblin, D. E., and Wenciewicz, T. A. (2019) Fimsbactin and Acinetobactin Compete for the Periplasmic Siderophore Binding Protein BauB in Pathogenic *Acinetobacter baumannii*. *ACS Chem. Biol.* 14, 674–687.
- (42) Mihara, K., Tanabe, T., Yamakawa, Y., Funahashi, T., Nakao, H., Narimatsu, S., and Yamamoto, S. (2004) Identification and Transcriptional Organization of a Gene Cluster Involved in Biosynthesis and Transport of Acinetobactin, a Siderophore Produced by *Acinetobacter baumannii* ATCC 19606T. *Microbiology* 150, 2587–2597.
- (43) Sheldon, J. R., and Skaar, E. P. (2020) *Acinetobacter baumannii* Can Use Multiple Siderophores for Iron Acquisition, but Only Acinetobactin is Required for Virulence. *PLoS Pathog.* 16, e1008995.
- (44) Shapiro, J. A., and Wenciewicz, T. A. (2016) Acinetobactin Isomerization Enables Adaptive Iron Acquisition in *Acinetobacter baumannii* through pH-Triggered Siderophore Swapping. *ACS Infect. Dis.* 2, 157–168.
- (45) Shapiro, J. A., and Wenciewicz, T. A. (2017) Structure-Function Studies of Acinetobactin Analogs. *Metallomics* 9, 463–470.
- (46) Griffiths, G. L., Sigel, S. P., Payne, S. M., and Neilands, J. B. (1984) Vibriobactin, a Siderophore from *Vibrio cholerae*. *J. Biol. Chem.* 259, 383–385.
- (47) Endicott, N. P., Lee, E., and Wenciewicz, T. A. (2017) Structural Basis for Xenosiderophore Utilization by the Human Pathogen *Staphylococcus aureus*. *ACS Infect. Dis.* 3, 542–553.
- (48) Windholz, T. B., and Johnston, D. B. R. (1967) Trichloroethoxycarbonyl: A Generally Applicable Protecting Group. *Tetrahedron Lett.* 8, 2555–2557.
- (49) Ree, H., Kim, J., Song, W. Y., Lee, J. E., and Kim, H. J. (2015) Total Syntheses and Evaluation of the Siderophore Functions of Fimsbactin B and Its Analogs. *B. Korean Chem. Soc.* 36, 1520–1523.
- (50) Kim, S., Lee, H., Song, W. Y., and Kim, H. J. (2020) Total Syntheses of Fimsbactin A and B and Their Stereoisomers to Probe the Stereoselectivity of the Fimsbactin Uptake Machinery in *Acinetobacter baumannii*. *Org. Lett.* 22, 2806–2810.
- (51) McKee, J. A. (1991) Iron Transport Mediated Drug Delivery. I. Synthesis and Biological Evaluation of Catechol Siderophore-Beta-Lactam Conjugates. II. Synthesis and Antifungal Activity of Hydroxamate Siderophore-Based Antifungal Conjugates. Ph.D. Dissertation, The University of Notre Dame, Notre Dame, IN.
- (52) Smith, R. M., and Martell, A. E. (1974) *Critical Stability Constants*, Vol. 1, Plenum Press, New York, NY.
- (53) Gaddy, J. A., Arivett, B. A., McConnell, M. J., López-Rojas, R., Pachón, J., and Actis, L. A. (2012) Role of Acinetobactin-Mediated Iron Acquisition Functions in the Interaction of *Acinetobacter baumannii* Strain ATCC 19606 with Human Lung Epithelial Cells, *Galleria mellonella* Caterpillars, and Mice. *Infect. Immun.* 80, 1015–1024.
- (54) Moynié, L., Serra, I., Scorciapino, M. A., Oueis, E., Page, M. G., Ceccarelli, M., and Naismith, J. H. (2018) Preacinetobactin Not Acinetobactin is Essential for Iron Uptake by the BauA Transporter of the Pathogen *Acinetobacter baumannii*. *eLife* 7, e42270.
- (55) Bailey, D. C., Bohac, T. J., Shapiro, J. A., Giblin, D. E., Wenciewicz, T. A., and Gulick, A. M. (2018) Crystal Structure of the Siderophore Binding Protein BauB Bound to an Unusual 2:1

Complex Between Acinetobactin and Ferric Iron. *Biochemistry* 57, 6653–6661.

(56) CLSI. (2012) Methods for Dilution Antimicrobial Susceptibility Tests for Bacteria That Grow Aerobically; Approved Standard. In *CLSI document M07-A9*, 9th ed.; Clinical and Laboratory Standards Institute, Wayne, PA.

(57) Song, W. Y., and Kim, H. J. (2020) Current Biochemical Understanding Regarding the Metabolism of Acinetobactin, the Major Siderophore of the Human Pathogen *Acinetobacter baumannii*, and Outlook for Discovery of Novel Anti-Infectious Agents Based Thereon. *Nat. Prod. Rep.* 37, 477–487.

(58) Allred, B. E., Correnti, C., Clifton, M. C., Strong, R. K., and Raymond, K. N. (2013) Siderocalin Outwits the Coordination Chemistry of Vibriobactin, a Siderophore of *Vibrio cholerae*. *ACS Chem. Biol.* 8, 1882–1887.

(59) Cass, M. E., Garrett, T. M., and Raymond, K. N. (1989) The Salicylate Mode of Bonding in Protonated Ferric Enterobactin Analogs. *J. Am. Chem. Soc.* 111, 1677–1682.

(60) Zhanel, G. G., Golden, A. R., Zelenitsky, S., Wiebe, K., Lawrence, C. K., Adam, H. J., Idowu, T., Domalaon, R., Schweizer, F., Zhanel, M. A., Lagacé-Wiens, P. R. S., Walkty, A. J., Noreddin, A., Lynch, J. P., III, and Karlowsky, J. A. (2019) Cefiderocol: A Siderophore Cephalosporin with Activity Against Carbapenem-Resistant and Multidrug-Resistant Gram-Negative Bacilli. *Drugs* 79, 271–289.

(61) Kim, A., Kutschke, A., Ehmann, D. E., Patey, S. A., Crandon, J. L., Gorseth, E., Miller, A. A., McLaughlin, R. E., Blinn, C. M., Chen, A., Nayar, A. S., Dangel, B., Tsai, A. S., Rooney, M. T., Murphy-Benenato, K. E., Eakin, A. E., and Nicolau, D. P. (2015) Pharmacodynamic Profiling of a Siderophore-Conjugated Monocarbam in *Pseudomonas aeruginosa*: Assessing the Risk for Resistance and Attenuated Efficacy. *Antimicrob. Agents Chemother.* 59, 7743–7752.

(62) Tomaras, A. P., Crandon, J. L., McPherson, C. J., Banevicius, M. A., Finegan, S. M., Irvine, R. L., Brown, M. F., O'Donnell, J. P., and Nicolau, D. P. (2013) Adaptation-based resistance to siderophore-conjugated antibacterial agents by *Pseudomonas aeruginosa*. *Antimicrob. Agents Chemother.* 57, 4197–4207.